

High-sampled structural displacement estimation through the FIR filter-based two-stage fusion of high-sampled acceleration and temporally aliased low-sampled displacement measurements

Zhanxiong Ma^a, Peipei Liu^b, Jaemook Choi^a, Hoon Sohn^{a,*}

^a Department of Civil and Environmental Engineering, Korea Advanced Institute of Science and Technology, Daejeon, South Korea

^b School of Civil Engineering, Southeast University, Nanjing, China

ARTICLE INFO

Communicated by Dionisio Bernal

Keywords:

Displacement estimation
Finite impulse response filter
Temporal aliasing
Vision camera
Accelerometer
Data fusion

ABSTRACT

This paper proposes an FIR filter-based two-stage fusion technique for high-sampled (HS) structural displacement estimation using HS acceleration and temporally aliased low-sampled (TLS) displacement measurements. First, the temporally aliased error in the TLS displacement measurement is estimated using the acceleration measurement and then eliminated to obtain an anti-aliased low-sampled (ALS) displacement. Next, a low-frequency displacement is estimated from the ALS displacement, and a high-frequency displacement is estimated from the HS acceleration measurement. Finally, the HS displacement is estimated by combining the estimated low- and high-frequency displacements. The proposed technique is also applied to estimate the HS structural displacement by fusing a vision camera and an accelerometer. An automated algorithm is proposed to estimate a scale factor for converting a translation in a pixel unit to a displacement in a length unit and to align measurements of two sensors using short-period HS acceleration and TLS vision measurements. The performance of the proposed technique was numerically and experimentally validated. A significant improvement in the displacement estimation accuracy was achieved compared to existing FIR filter-based techniques owing to the explicit elimination of the temporally aliased error.

1. Introduction

In civil engineering, structural failures can lead to catastrophic results, and structural health must be continuously monitored to prevent such failures. Structural health monitoring aims to monitor, analyze, and identify various types of loads and structural responses of a target structure during its service life. This enables the assessment of the structural performance and safety status. The displacement response plays a vital role in structural health monitoring because it helps to understand the global behavior of structures and evaluate structural safety and can be used in structural control and disaster prevention and mitigation.

Several structural displacement sensing techniques using accelerometers [1,2], real-time kinematic global navigation satellite systems (RTK-GNSS) [3], strain sensors [4,5], radar systems [6,7], and vision cameras [8–11] have been proposed. However, each of these sensors has advantages and disadvantages. For example, displacement can be easily calculated by the double integration of

* Corresponding author.

E-mail addresses: mazhanxiong@kaist.ac.kr (Z. Ma), peipeiliu@seu.edu.cn (P. Liu), cjmoock@kaist.ac.kr (J. Choi), hoonsohn@kaist.ac.kr (H. Sohn).

accelerometer measurements; but, a low-frequency drift appears in the acceleration-based displacement. Displacement can also be estimated using vision cameras; however, vision-based displacement suffers from limited accuracy and sampling rate. Another trend for structural displacement estimation is to fuse multiple types of sensors for improved displacement estimation, which includes the fusion of the accelerometer with other sensors such as RTK-GNSS [12,13], strain sensors [14], vision cameras [15–18], radar systems [19], and inclinometers [20]. Notably, the fusion of accelerometer with other sensors can improve accuracy and increase sampling rate of the estimated displacement.

The fusion of accelerometer with other sensors has been extensively studied by using either finite impulse response (FIR) filters or Kalman filters. Kalman filters are advantageous for real-time displacement estimation without any time delay. However, they are essentially infinite impulse response (IIR) filters and therefore have the limitations of IIR filters, such as nonlinear phase [21], which introduces additional errors in the estimated displacement. Although FIR filters have a linear phase, it introduces a little time delay in the displacement estimation. In addition, the cutoff frequency required for FIR filters can be determined more easily than the noise variation required for Kalman filters. If real-time estimation capability is important in certain applications (e.g., structural control), then Kalman filters should be chosen. However, in the authors' experience, FIR filters outperform Kalman filters in terms of displacement estimation accuracy, and if a short time delay for displacement estimation is acceptable, then FIR filters should be selected for data fusion.

FIR filters have been used to fuse the acceleration and displacement measurements [14,15,18,20,22]. Fig. 1 presents an overall flowchart of the existing FIR filter-based structural displacement estimation technique that uses high-sampled (HS) acceleration and low-sampled (LS) displacement measurements. The HS displacement is first estimated from the HS acceleration measurement using double integration with a large low-frequency drift. The drifted HS displacement is then high-pass filtered to extract the HS high-frequency displacement. Meanwhile, an LS low-frequency displacement is first extracted from the LS displacement measurement using a low-pass filter and then upsampled to match the sampling rate of the acceleration measurement to obtain an HS low-frequency displacement. The final HS displacement is estimated by combining the HS low- and high-frequency displacements. Note that the low- and high-pass filters employed here are complementary, and the cut-off frequency (f_c) of the filters is determined as the first natural frequency of a target structure [14,22,23] or based on the noise characteristics of acceleration and displacement measurements [15,18,20].

However, temporal aliasing may occur in the LS displacement measurement with the existence of displacement above its Nyquist frequency (f_N), that is, half of its sampling rate (F_L). Because the LS displacement measurement only contributes to the low-frequency ($< f_c$) components of the final estimated displacement, an aliased error above f_c in the LS displacement measurement has no effect on the final estimated displacement; however, an aliased error below f_c is retained in the final estimated displacement, thereby causing inaccurate displacement estimation. The aliasing issues can be addressed by applying an anti-aliasing filter before original analog signals are converted to digital converter, which eliminates displacement components with frequencies above f_N . However, this method is only applicable when LS displacement measurements are originally recorded in an analog format. For displacement measurements obtained from radar, RTK-GNSS, or vision cameras, it's not possible to use an anti-aliasing filter. Some techniques have attempted to address the temporal aliasing issue when using non-uniform [24] or uniform [25] low-sampling vision measurements, but they only focus on structural modal identification.

In this study, an FIR filter-based two-stage fusion technique is proposed to estimate HS displacement using HS acceleration and temporally aliased LS (TLS) displacement measurements. First, the temporally aliased error in the TLS displacement measurement is estimated from the acceleration measurement and then eliminated from the TLS displacement measurements to obtain an anti-aliased LS (ALS) displacement. Next, an HS low-frequency displacement is estimated from the ALS displacement, and the HS high-frequency displacement is estimated from the acceleration measurement. Finally, the HS displacement is estimated by combining the estimated HS low-frequency and high-frequency displacements. The proposed FIR filter-based two-stage fusion technique is applied to estimate the HS structural displacement using a vision camera and an accelerometer. Using short-period HS acceleration and TLS vision measurements, an initial calibration algorithm is proposed to achieve (1) the automated estimation of a scale factor for unit conversion

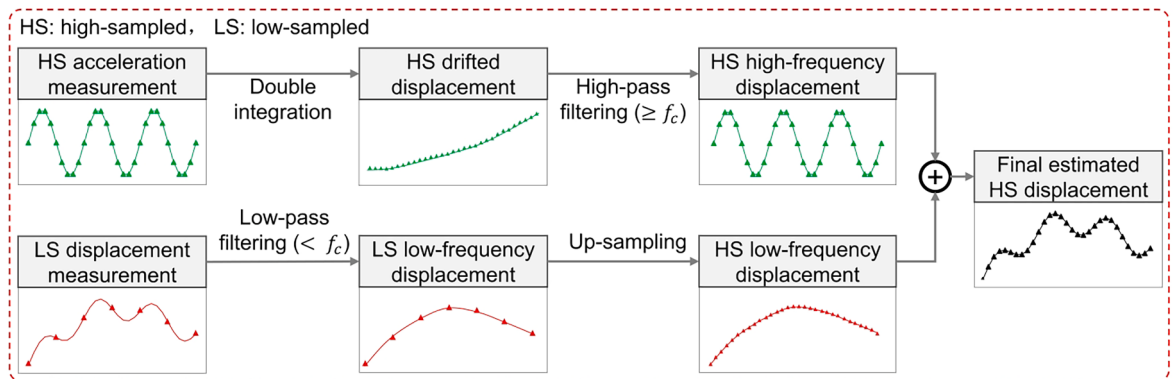


Fig. 1. Existing FIR filter-based fusion of high-sampled (HS) acceleration and low-sampled (LS) displacement measurements for structural displacement estimation.

and (2) the precise alignment of vision and acceleration measurements. This study offers the following contributions: (1) an FIR filter-based two-stage fusion technique is proposed for HS structural displacement estimation using HS acceleration and TLS displacement measurements; (2) by explicitly eliminating the temporally aliased error in the TLS displacement measurement, the displacement estimation accuracy is significantly improved compared to existing FIR filter-based techniques; (3) the proposed FIR filter-based two-stage fusion technique is applied to vision cameras and accelerometers, and HS structural displacement is estimated using HS acceleration and TLS vision measurements; and (4) precise alignment of vision and acceleration measurements and estimation of scale factor are automatically achieved using short-period HS acceleration and TLS vision measurements. Note that the authors previously explored the fusion of strain gauges and accelerometer [26] and the fusion of millimeter-wave radar and accelerometer [19], but both strain and radar measurements were obtained at the same high sampling rate as acceleration measurements. Therefore, an existing FIR filter [22] was directly adopted without any temporal aliasing issue.

The remainder of this paper is organized as follows. The proposed FIR filter-based two-stage fusion technique is described in [Section 2](#), and its application to fuse vision cameras and accelerometers is described in [Section 3](#). The performance of the proposed technique is first examined using numerical simulation of a simply supported beam model, as illustrated in [Section 4](#), followed by experimental validation, as illustrated in [Section 5](#). The concluding remarks are presented in [Section 6](#).

2. Development of an FIR filter-based two-stage fusion technique for HS displacement estimation using HS acceleration and TLS displacement measurements

2.1. Review of temporal aliasing phenomena

According to the Nyquist-Shannon sampling theorem [27], the temporal aliasing phenomena may occur in the LS displacement measurement with the existence of displacement above its Nyquist frequency (f_N), that is, half of its sampling rate (F_L). To intuitively understand the aliasing phenomena, the “fanfold paper” method [28] is commonly used. As shown in [Fig. 2](#), the frequency spectrum of actual displacement is plotted on a small stack of semitransparent fan-fold paper with folds in the vertical direction. The frequency axis from left to right has inward creases at multiples of f_N , and the outward creases at odd multiples of f_N . When sampling the actual displacement with a sampling frequency of F_L (i.e., downsampling from infinite to F_L), the stack of fanfold paper simply collapses, and the components above f_N are “folded” down into the frequency band of $[0, f_N]$, which represents the exact frequency spectrum of the LS displacement measurement. All frequency components from the high-frequency region ($>f_N$) are called aliasing errors.

2.2. Working principle of the proposed FIR filter-based two-stage fusion technique

In this section, an FIR filter-based two-stage fusion technique is proposed for HS structural displacement estimation using HS acceleration and TLS displacement measurements. A temporally aliased error in the TLS displacement measurement is first estimated using acceleration measurement and then eliminated from the TLS displacement measurement to estimate the ALS displacement. Finally, the low-frequency component of the estimated ALS displacement and high-frequency component of the acceleration-based displacement are combined to estimate the HS displacement. The proposed technique, as shown in [Fig. 3](#) includes the following two stages.

Stage I—TLS displacement anti-aliasing: First, an HS drifted displacement is estimated from the HS acceleration measurement sampled at F_H via double integration, and a high-pass filter (P_H) with a cut-off frequency of f_N is applied to the HS drifted displacement to extract the HS displacement with a frequency above f_N (hereafter denoted as HS above- f_N displacement). Here, f_N denotes the Nyquist frequency of the TLS displacement measurement, that is, half of the sampling rate ($f_N = F_L/2$). Because P_H is used for anti-aliasing, it is hereafter referred to as an anti-aliasing filter. Next, the HS above- f_N displacement is downsampled to the sampling rate of the TLS displacement measurement (F_L), and then an LS temporally aliased error is estimated. Finally, the estimated LS temporally aliased error is eliminated from the TLS displacement measurement to obtain an ALS displacement sampled at F_L .

Stage II—HS displacement estimation: First, a pair of complementary filters, including high- and low-pass filters (Q_H and Q_L , respectively), are applied to the HS drifted displacement and estimated ALS displacement to extract the HS high- and low-frequency displacements, respectively. Note that the estimated ALS displacement is upsampled to F_H before filtering. The details regarding the cut-off frequency (f_c) of the complementary filters are explained in [Section 2.2](#). The HS displacement is finally estimated by combining the extracted HS low- and high-frequency displacements.

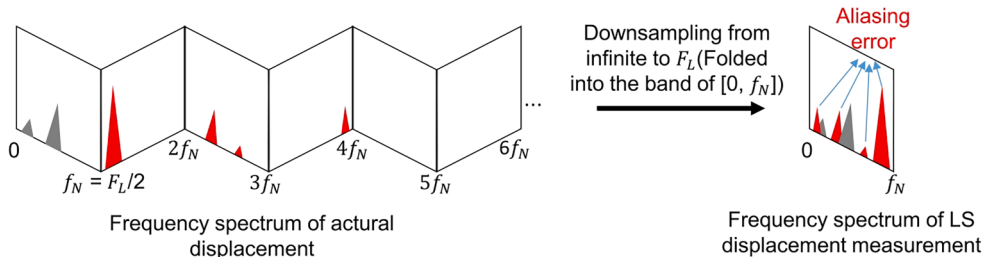


Fig. 2. A straightforward illustration of temporal aliasing phenomena using a “fanfold paper” method.

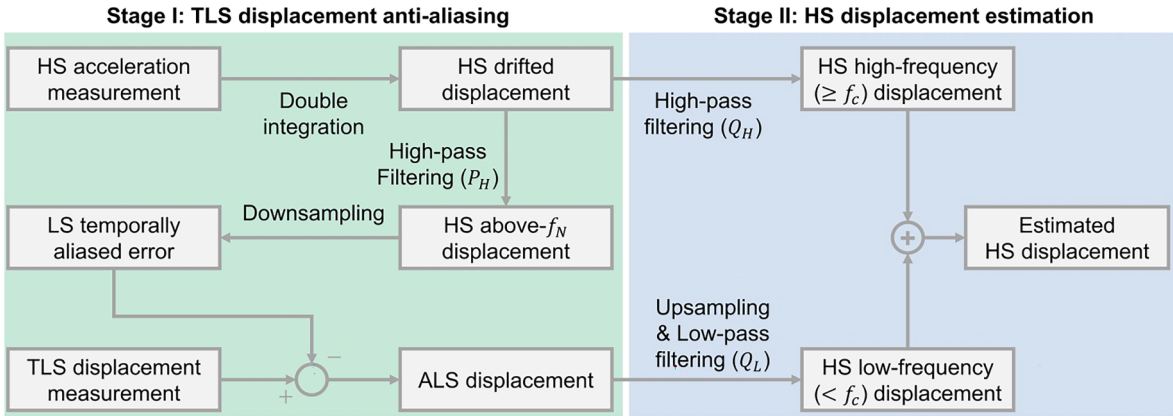


Fig. 3. Proposed two-stage FIR filter-based fusion of HS acceleration and TLS displacement measurements for HS structural displacement estimation.

In the proposed technique, the temporal aliasing error in TLS displacement measurement is estimated as the downsampled acceleration-based displacement after removing the displacement component with frequency below f_N . This is further justified in Fig. 4 using the “fanfold paper” method. The downsampling process collapses the stack of fanfold paper and components above f_N are “folded” down into the frequency band of [0 Hz, f_N], which represents the frequency spectrum of aliasing errors in the TLS displacement measurement. It should be noted that the sampling frequency of acceleration measurement (F_H) are assumed to be sufficiently high so that no temporal aliasing exists in the acceleration measurement.”

2.3. FIR filter design and parameter determination

The proposed FIR filter-based two-stage fusion technique is described in Section 2.2, and consists of an anti-aliasing filter (P_H) and a pair of complementary filters (Q_L and Q_H). An example of the frequency transfer functions of P_H , Q_L , and Q_H is shown in Fig. 5. Note that, here, the ripples in both the pass and stop bands are ignored to focus on the transition bands.

P_H is used to extract displacement components with the frequency above f_N from HS drifted displacement estimated from acceleration measurement, and therefore, the cut-off frequency of P_H need to be set to f_N in ideal conditions as shown in Fig. 6(a). However, an actual filter has a transition band with the ripples in both the pass and stop bands (Fig. 6(b)), and one more parameter, i.e., the transition bandwidth, needs to be determined. Assuming that the cut-off frequency of Q_L and Q_H is set to f_c , the ALS displacement contributes only to the low-frequency (< f_c) component of the final estimated displacement, and therefore it must include correct information up to f_c . Then, P_H should be able to completely remove displacement with the frequency below f_c , and its bandwidth needs to be smaller than or equal to ($f_N - f_c$). This statement is further justified in Fig. 7. When the transition bandwidth of P_H is larger than ($f_N - f_c$), the ALS displacement has distorted displacement in the frequency band below f_c , which will cause inaccurate final displacement estimation. Note that the distortion in the frequency band above f_c does not affect the final estimated HS displacement because the ALS displacement is further filtered by Q_L to retain only the low-frequency (< f_c) displacement component. Considering that a sharp transition band leads to a large order of the filter (i.e., a long time delay and phase distortion) and serious fluctuations (i.e., large ripples) in both the pass and stop bands owing to the Gibbs phenomenon [29] (Fig. 6(b)), the transition bandwidth of P_H should be maximized to minimize these fluctuations and time delays. Therefore, its transition bandwidth is set to ($f_N - f_c$). The minimum bandwidth is suggested to be 0.5 Hz in this study and then f_N should be at least larger than ($f_c + 0.5$ Hz), indicating that the smallest sampling rate required for the TLS displacement measurement is,

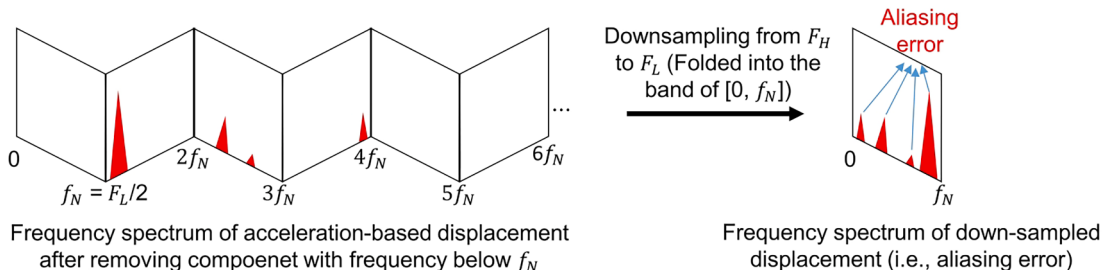


Fig. 4. A straightforward illustration of the estimation of temporal aliasing error from acceleration-based displacement using a “fanfold paper” method.

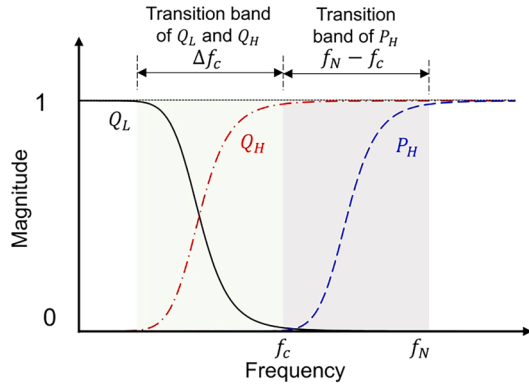


Fig. 5. Example of FIR complementary filters (Q_L and Q_H) and anti-aliasing filter (P_H).

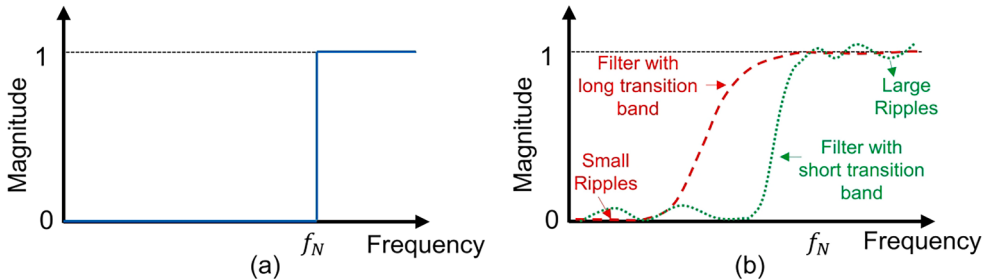


Fig. 6. Comparison between (a) ideal and (b) actual filters.

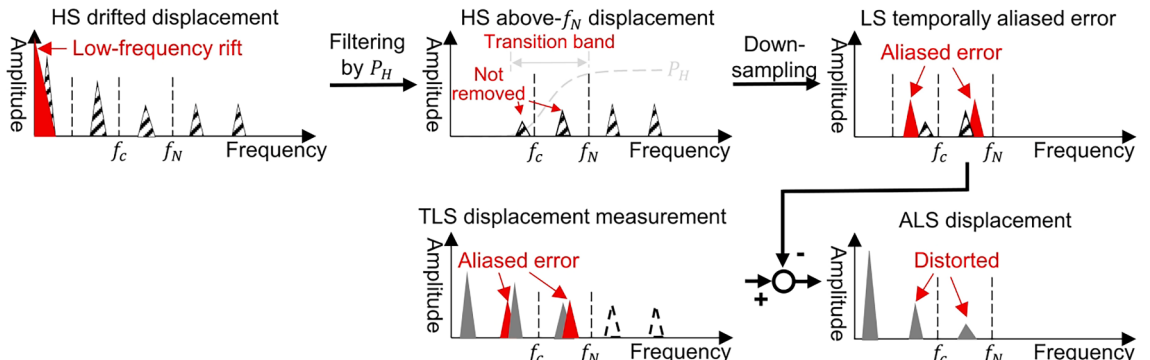


Fig. 7. Distortion issue of ALS displacement when using a P_H with transition bandwidth larger than $(f_N - f_c)$.

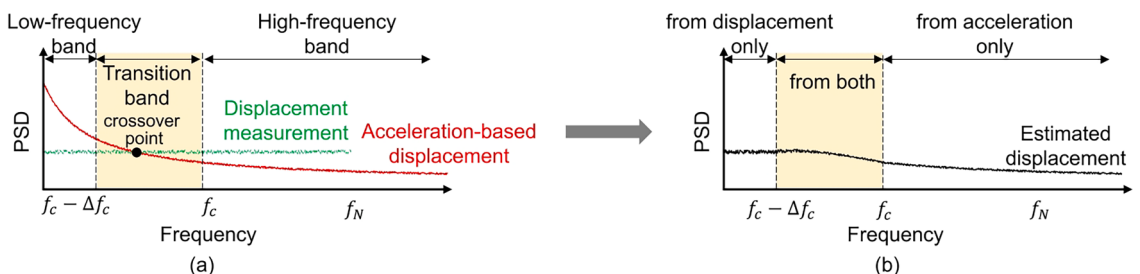


Fig. 8. Example of noise power spectral densities (PSD) of (a) acceleration-based displacement and displacement measurement and (b) the correspondingly estimated displacement.

$$F_{\min,I} = 2(f_c + 0.5) \quad (1)$$

The cut-off frequency (f_c) and transition band (Δf_c) of Q_L and Q_H should be determined based on the noise characteristics of the acceleration and displacement measurements. Fig. 8(a) shows the typical noise power spectral densities (PSD) of acceleration-based displacement and displacement measurements. The displacement measurement has a uniform noise level, whereas the acceleration-based displacement is estimated from the double integration of acceleration measurement and has a decreasing noise distribution as the frequency increases. Normally, there is a crossover point between noise spectra. To minimize the noise in the estimated HS displacement (Fig. 8(b)), the transition band need to include the crossover point and the value of $(f_c - \Delta f_c)$ should be sufficiently large to completely remove the low-frequency drift of the acceleration-based displacement. The value of $(f_c - \Delta f_c)$ relies on the low-frequency performance of an accelerometer and it varies depending on different types of accelerometers. However, a series of laboratory tests have been conducted by the authors using force-balance type and high-cost and low-cost MEMS type accelerometers, and it is concluded that a value of 0.5 Hz is universally good for these accelerometers. The value of Δf_c should be sufficiently small to include more high-frequency components of the acceleration-based displacement in the estimated HS displacement, thereby achieving a better displacement estimation accuracy. However, a sharp transition band leads to a large order of the filter (i.e., a long time delay and phase distortion) and serious fluctuations in both the pass and stop bands owing to the Gibbs phenomenon [29], and therefore the transition bandwidth (Δf_c) is suggested to be 0.5 Hz. Note that because the transition bands of the filters used in existing studies [15,22,23,30] cannot be explicitly controlled, this study designed P_H and Q_L and Q_H as Equiripple-type FIR filters using the MATLAB Filter Designer Toolbox [31] with determined cut-off frequency and transition bandwidths.

Fig. 9 presents a spectral interpretation of the proposed two-stage FIR filter-based fusion technique considering the transition bands of the filters. The displacement in the frequency band of $[f_c, f_N]$ is not completely removed by P_H owing to its transition band (Fig. 9(c)) and is partially retained in the estimated LS error (Fig. 9(d)). Therefore, the ALS displacement in the frequency band of $[f_c, f_N]$ is distorted after Stage I-4, as shown in Fig. 9(f). However, it has no effect on the final estimated HS displacement because Q_L retains only the low-frequency ($< f_c$) displacement of the ALS displacement (Fig. 9(h)). Owing to the presence of the transition band of the complementary filters, the acceleration measurement completely contributes to the portion of the estimated HS displacement with frequencies higher than f_c , whereas the displacement measurement completely contributes to the portion of the estimated HS displacement with frequencies lower than $f_c - \Delta f_c$. Between $f_c - \Delta f_c$ and f_c , both acceleration and displacement measurements contribute to the estimated HS displacements (Fig. 9(i)).

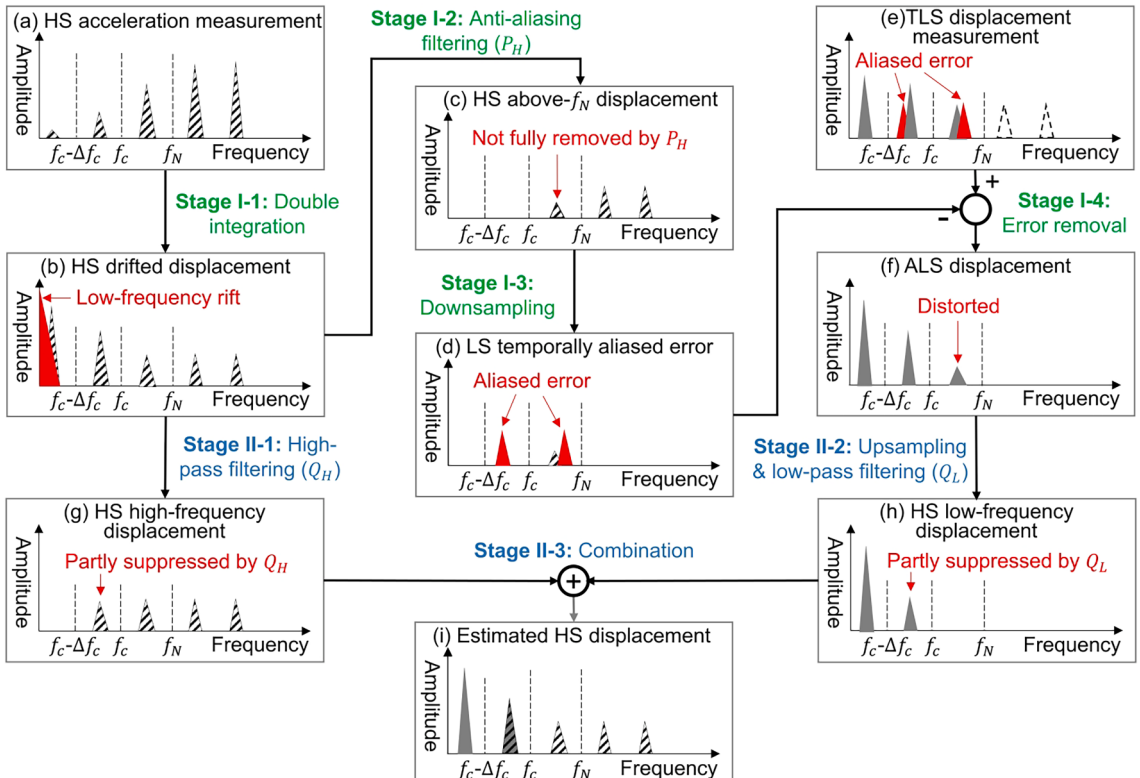


Fig. 9. Spectral interpretation of the proposed two-stage FIR filter-based fusion technique considering the transition bands of filters.

3. Application of the proposed technique to fuse an accelerometer and a vision camera for HS displacement estimation

The two-stage FIR-filter fusion technique proposed in Section 2 was applied to fuse a vision camera and an accelerometer, and the overall scheme of displacement estimation is shown in Fig. 10. A vision camera installed on a structure tracks a nearby fixed target with a low sampling rate ($F_{s,v}$), and an accelerometer is placed at the same location as that of the vision camera to measure the acceleration of the structure with a high sampling rate ($F_{s,a}$). Assuming that the structure has a displacement with a frequency above $F_{s,v}/2$, a TLS displacement is first estimated from vision measurement and then is fused with HS acceleration measurement using the proposed FIR filter-based two-stage fusion technique to obtain an HS displacement. Among several available computer vision algorithms [32–34] for vision-based displacement estimation, a template-matching algorithm based on zero-mean normalized cross-correlation (ZNCC) [34] was adopted in this study. A rectangular subset image of size $M \times N$ pixels, i.e., Template T , was first selected from the first frame by including a target. Then, a ZNCC matrix can be constructed between the template and the rectangular subset images from the current frame I at location (x, y) with the size of $M \times N$ pixels ($I_c(x, y)$),

$$\text{ZNCC}(x, y) = \frac{\sum_{j=1}^N \sum_{i=1}^M \{I(x+i, y+j) - \mu(I_c(x, y))\} \{T(i, j) - \mu(T)\}}{\sqrt{\sum_{j=1}^N \sum_{i=1}^M \{I(x+i, y+j) - \mu(I_c(x, y))\}^2 \sum_{j=1}^N \sum_{i=1}^M \{T(i, j) - \mu(T)\}^2}} \quad (2)$$

where $\mu(I_c(x, y))$ and $\mu(T)$ denote the mean values of $I_c(x, y)$ and T , respectively. The target location at the current frame I can be estimated by finding the maximum value of the ZNCC matrix, but it only has pixel-level resolution. Therefore, the ZNCC matrix is spline interpolated to achieve subpixel resolution in target location estimation. The variation of target location becomes structural translation in pixel units, which is further converted to structural displacement in length units using a pre-estimated scale factor.

However, two issues should be addressed in advance: (1) accelerometer and vision camera measurements may not be perfectly aligned, and (2) the estimation of the scale factor requires manual measurement of the target physical size, which may not be easy in practice. Fig. 11 presents an automated initial calibration algorithm for the measurement alignment and scale factor estimation using short-period (less than 1 min) HS acceleration and TLS vision measurements, and it consists of four steps:

Step 1: A TLS translation is first estimated from the vision measurement using the template-matching algorithm, and a band-pass filter is then applied to the estimated TLS translation to obtain a filtered translation. Notably, the filtered translation includes a temporally aliased error (Fig. 11(a)).

Step 2: An HS displacement is estimated from the acceleration measurement by double integration and then downsampled to $F_{s,v}$ to obtain a TLS displacement. Subsequently, a bandpass filter is applied to the acceleration-based TLS displacement to obtain a filtered displacement. Notably, the filtered displacement includes a temporally aliased error (Fig. 11(b)).

Step 3: The cross-correlation function between the filtered displacement and translation is calculated using the MATLAB built-in function *xcorr* [35], and the time lag between the vision and acceleration measurements is estimated. However, the initial time lag is only discrete, with an interval of $1/F_{s,v}$, which may be insufficient. Thus, spline interpolation was applied to the cross-correlation function to estimate a more precise time lag (Fig. 11(c)).

Step 4: The filtered translation and displacement are precisely aligned with the estimated time lag, and the scale factor is estimated by applying the least square estimate algorithm to the aligned and filtered translation and displacement (Fig. 11(d)).

The key parameter associated with the algorithm is the cut-off frequency of the band-pass filter. The lower value should be sufficiently large to eliminate the low-frequency drift in the acceleration-based displacement, and its value was set to 0.5 Hz in this study. The upper value is suggested to be $F_{s,v}/10$. However, it can be set to $F_{s,v}/2$, with a rather small $F_{s,v}$.

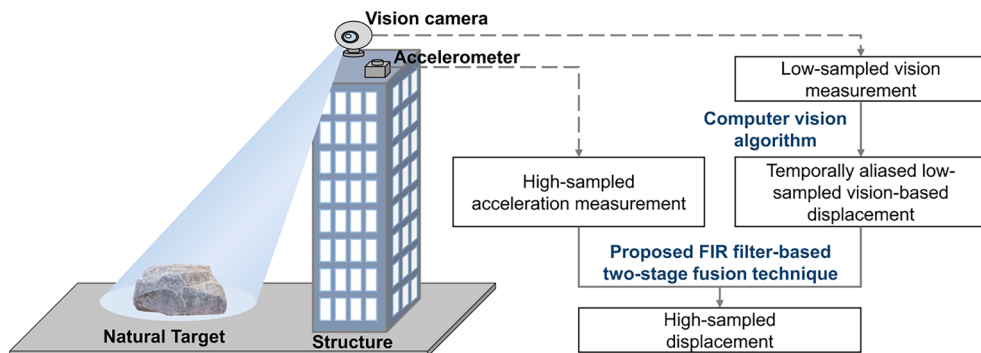


Fig. 10. Overall scheme of fusing a vision camera and an accelerometer for HS structural displacement estimation using the proposed FIR filter-based two-stage fusion technique.

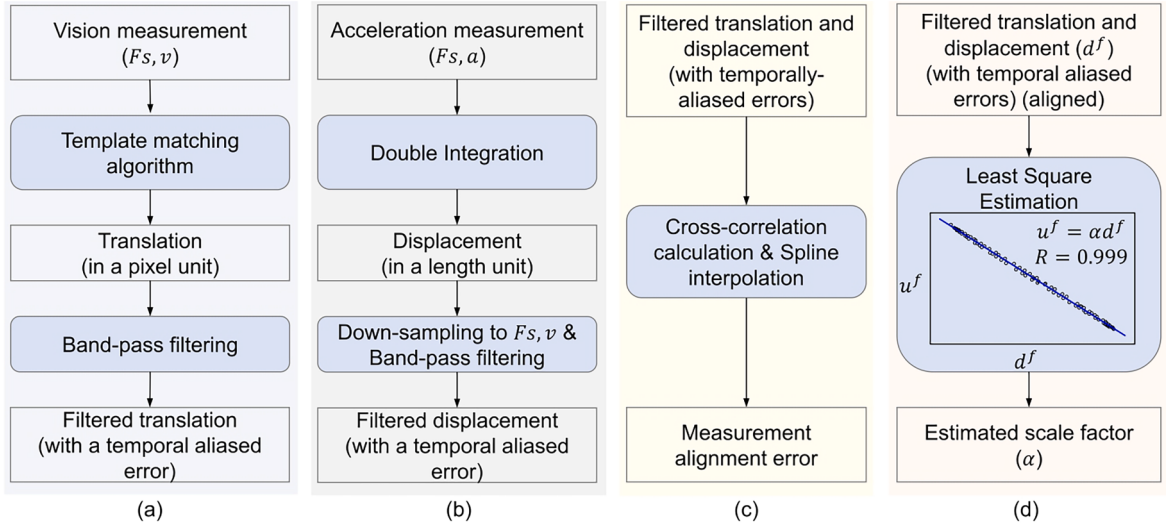


Fig. 11. Flowchart of the proposed initial calibration for automated scale factor estimation and measurement alignment: (a) step 1: estimation of a band-pass filtered translation in a pixel unit from the vision measurement, (b) step 2: estimation of a band-pass filtered displacement in a length unit from the acceleration measurement, (c) step 3: estimation of an alignment error between vision and acceleration measurements, and (d) step 4: estimation of a scale factor for unit conversion.

4. Numerical validation

4.1. Simulation description

A simply supported beam with a length of 40 m was simulated in MATLAB to validate the displacement estimation performance of the proposed technique (Fig. 12(a)). The beam had a uniform rectangular cross-section with a width of 3 m and height of 1 m. The flexural rigidity and mass per unit length of the beam were $6.03 \times 10^{10} \text{ N/m}^2$ and $1.5 \times 10^3 \text{ kg/m}$, respectively. A concentrated excitation force with a duration of 100 s (Fig. 12(b)) was applied to the center of the beam. Note that the excitation force includes a pseudo-static component and several sinusoidal (0.7 Hz, 3.1 Hz, 8 Hz, and 10.3 Hz) components. The displacement and acceleration responses under the excitation force were simulated at the same location with a sampling rate of 100 Hz using the Newmark- β method [36].

The simulated displacement was downsampled to 10 Hz, and the downsampled (i.e., TLS) displacement was fused with the acceleration sampled at 100 Hz (i.e., HS) for HS displacement estimation. Note that Gaussian noise was added to the acceleration and downsampled displacement to simulate measurement noise, and the signal-to-noise ratios (SNRs) were 40. Fig. 13 shows a comparison of the frequency spectra of the displacements sampled at 100 Hz and 10 Hz. Two temporally aliased errors (0.3 Hz and 2 Hz) are clearly observed in the displacement sampled at 10 Hz.

4.2. Displacement estimation results

The transition bands of the complementary filters (Q_L and Q_H) and anti-aliasing filter (P_H) were set to [0.5 Hz, 1 Hz] and [1 Hz, 5 Hz], respectively. An existing technique [22] was adopted for performance comparison, and the cut-off frequency was set to 1 Hz with an accuracy index of 0.97. Note that though there are more recent studies on the FIR-filter-based displacement estimation [18,37,38],

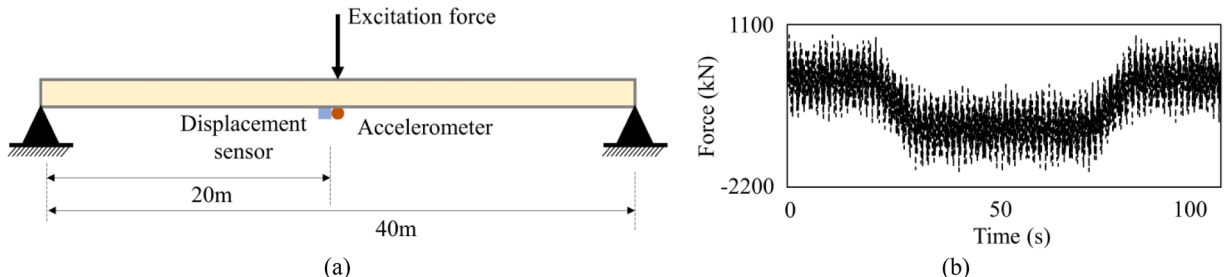


Fig. 12. (a) Overview of a numerical simply-supported beam and (b) an excitation force signal applied to the center of the beam.

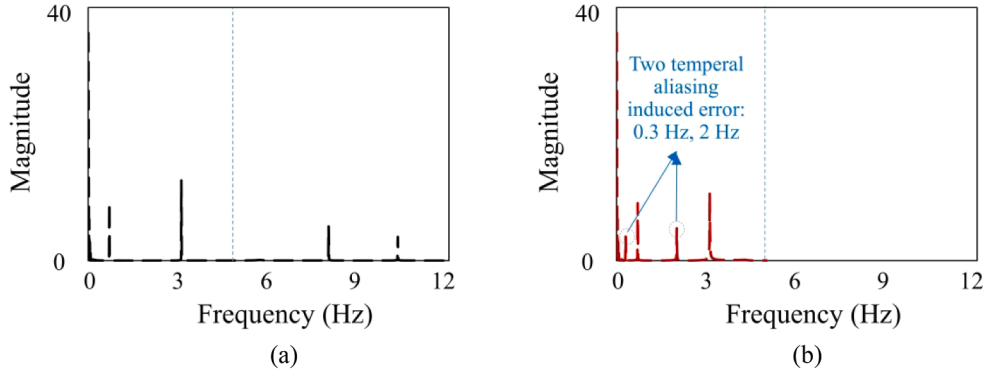


Fig. 13. Frequency spectra of (a) HS (100 Hz) and (b) downsampled (10 Hz) displacements.

they adopted the FIR filter presented in this paper [22] or its variant[30]. Fig. 14 shows a comparison of the displacements estimated using the proposed and existing techniques, and they are in good agreement with the reference displacement (i.e., the originally simulated displacement). Additionally, the estimated displacements between 75 s and 80 s were zoomed in. A discrepancy was observed between the displacement estimated using the existing technique and the reference displacement. The root mean square errors (RMSEs) of the estimated displacements were calculated to quantitatively evaluate the performance of the two techniques. The RMSEs were reduced by 78 % using the proposed technique compared with the existing technique.

Fig. 15 depicts the frequency spectra of the estimated and reference displacements to clearly demonstrate the superiority of the proposed technique over the existing technique. The frequency spectrum of the displacement estimated using the proposed technique was in good agreement with that of the reference displacement. However, the temporally aliased error at 0.3 Hz in the TLS displacement was retained in the displacement estimated using the existing technique, causing a large RMSE. Notably, the existing technique eliminated the temporally aliased error at 2 Hz because only the low-frequency (<1 Hz) component of the TLS displacement was retained in the final estimated displacement. The excitation frequencies identified by the proposed and existing techniques were identical to those identified from the reference displacements and the nominated excitation frequencies. Note that, both the estimated

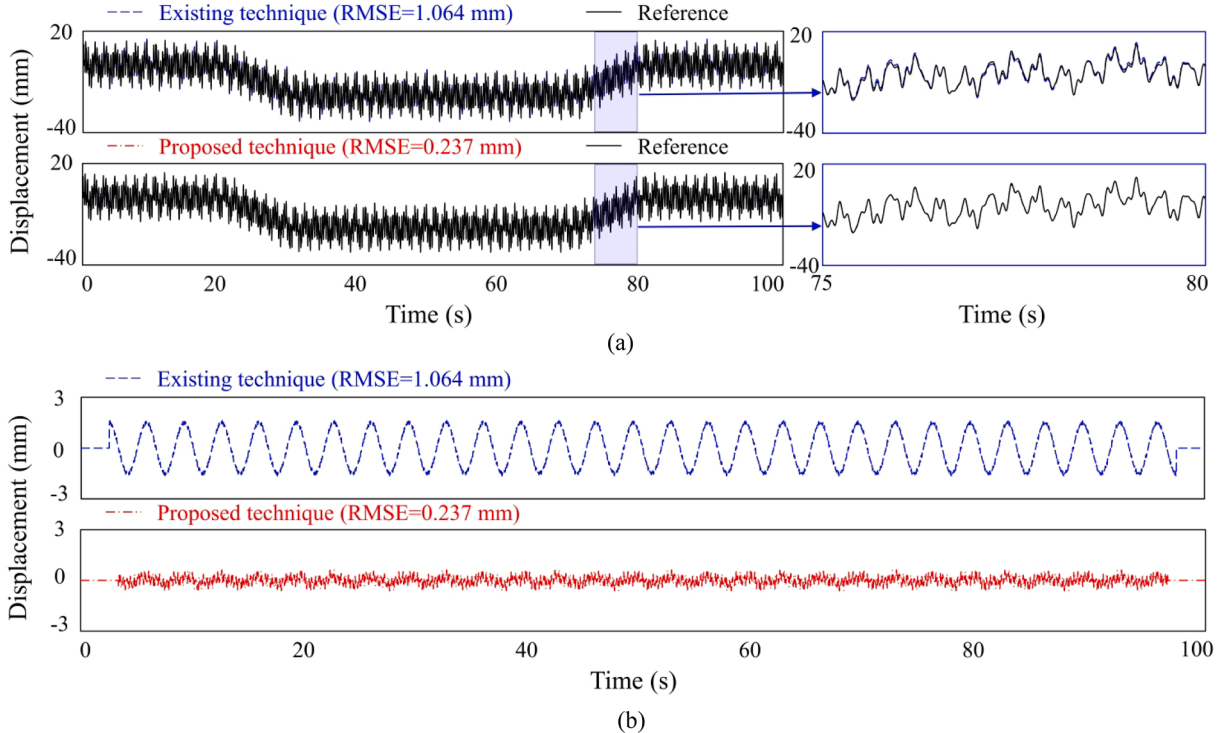


Fig. 14. Comparison of simply supported beam displacements estimated by the existing and proposed techniques using 10 Hz displacement and 100 Hz acceleration measurement: (a) estimated displacements and (b) corresponding errors.

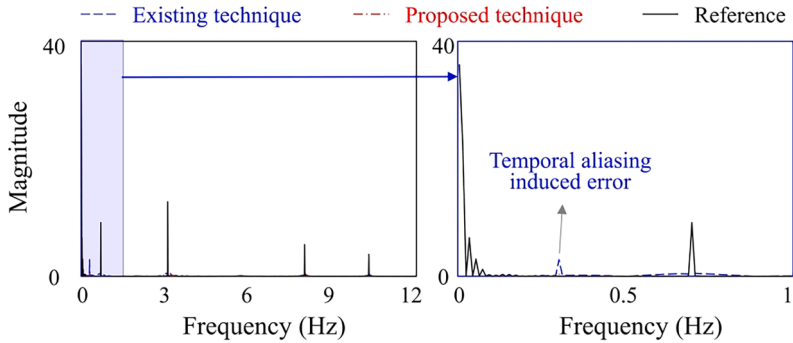


Fig. 15. Comparison of frequency spectra of simply supported beam displacement estimated by the existing and the proposed techniques using 10 Hz displacement and 100 Hz acceleration measurement.

and reference displacements had the same sampling rate of 100 Hz, so they share the same frequency resolution of 0.01 Hz.

4.3. Effect of measurement noise and measurement alignment error on displacement estimation performance

In addition, the effect of measurement noise on displacement estimation performance was investigated. The displacements were estimated by the proposed and existing techniques using the acceleration measurement with a fixed SNR of 40 and displacement measurement with an SNR varying from 20 to 100. The corresponding RMSEs are shown in Fig. 16(a). For the proposed technique, the RMSE was reduced to approximately 45 % when the SNR of the displacement measurement was increased from 20 to 30. Thereafter, increasing the SNR did not significantly reduce the RMSE. Because the displacements estimated by the existing technique had large RMSEs owing to temporally aliased errors, they were less sensitive to the SNR of the displacement measurement.

In this simulation, the acceleration and downsampled displacements were exactly aligned, which may not be possible in real-world applications. The effect of the measurement alignment error between the acceleration and displacement measurements on the displacement estimation performance was further studied, as shown in Fig. 16(b). Different measurement alignment errors were introduced and the corresponding displacements were estimated using the proposed and existing techniques. The displacement estimation errors of both techniques dramatically increased with increased measurement alignment errors, even less than 0.01 s, thus demonstrating the importance of precise measurement alignment.

5. Experimental validation using a vision camera and an accelerometer

5.1. Indoor single-story building test

5.1.1. Experimental setup

A single-story building model was used to validate the proposed technique, as shown in Fig. 17. An accelerometer (EpiSensor ES-U2) and a vision camera (DJI OSMO Action) were installed at the top of the model, and a shaker (ELECTRO-SEIS APS-400) moved the model in the horizontal direction. Table 1 lists the detailed specifications of the accelerometer and vision camera. The displacement of the model measured by a Polytech PSV-400 laser Doppler vibrometer (LDV) with a resolution of 0.5 pm [39] was used as the ground truth. The vision measurement was initially sampled at 30 (≈ 29.97) Hz, whereas both acceleration and LDV measurements were sampled at 100 Hz. Fig. 17 shows the field of view (FOV) of the vision camera and the selected region of interest (ROI). The distance

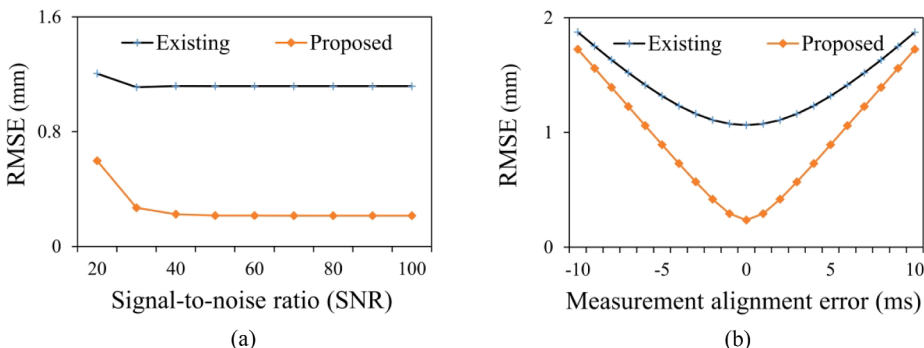


Fig. 16. Effect of (a) SNR of displacement measurement and (b) measurement alignment error on displacement estimation accuracy.

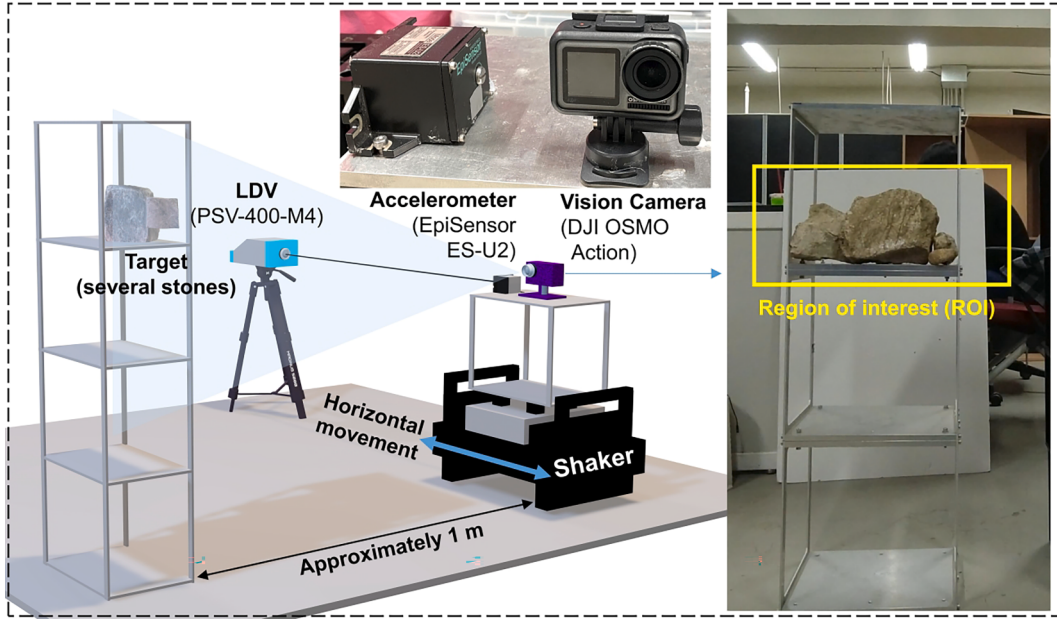


Fig. 17. Overall configuration of an indoor single-story building model test.

Table 1

Detailed specifications of the accelerometer and vision camera used in a single-story building model test.

| Sensors | Parameters | Values |
|------------------------------------|--|--|
| Accelerometer (EpiSensor ES-U2) | Type Dynamic range Bandwidth Full-scale range Operating temperature Hysteresis Linearity Cross-axis sensitivity Zero point thermal drift | Uniaxial force-balance 155 dB+ DC – 200 Hz $\pm 0.25 \text{ g}$ to $\pm 4 \text{ g}$ (User selectable) $-20 \sim 70^\circ \text{C}$ $< 0.1\%$ of full scale $< 1000 \mu\text{g/g}^2$ $< 1\%$ (including misalignment) $< 500 \mu\text{g}/^\circ\text{C}$ |
| Vision camera (DJI OSMO Action) | Sensor type Effective pixels Maximum aperture of lens Angle of view Resolution Sampling rate/frame per second | 1/2.3" type CMOS sensor 12 megapixels f/2.8 145° Up to 4 K (3840×2160) up to 60 Hz with 4 K resolution |

between the vision camera and the target, *that is*, several stones, was approximately 1 m. Five different sinusoidal signals were input into the shaker to excite the model in this test: (1) Excitation 1: 0.1 Hz + 2.2 Hz, (2) Excitation 2: 0.1 Hz + 3.3 Hz, (3) Excitation 3: 0.1 Hz + 5.1 Hz, (4) Excitation 4: 0.1 Hz + 6.3 Hz, and (5) Excitation 5: 0.1 Hz + 10.3 Hz.

5.1.2. Scale factor and displacement estimation results

First, an initial calibration was conducted using vision and acceleration measurements under Excitation 1 to estimate the scale factor and align the vision and accelerometer measurements. Fig. 18 presents the scale factor estimated using 100 Hz acceleration and 30 Hz vision measurements. The cut-off frequencies of the bandpass filter were set to [0.5 Hz, 3 Hz]. As there was no temporal aliasing, identical results were obtained using the proposed and existing algorithms [16].

Fig. 19(a) and (b) present the scale factors estimated by the two algorithms using 100 Hz acceleration and 3 Hz vision measurements. The cut-off frequencies of the bandpass filter were set to [0.5 Hz, 1.5 Hz]. The proposed algorithm still estimated the scale factor

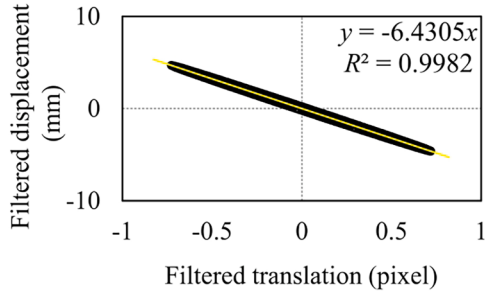


Fig. 18. Scale factors estimated using 100 Hz acceleration measurement and 30 Hz (not aliased) vision measurements (Excitation 1: 0.1 Hz + 2.2 Hz).

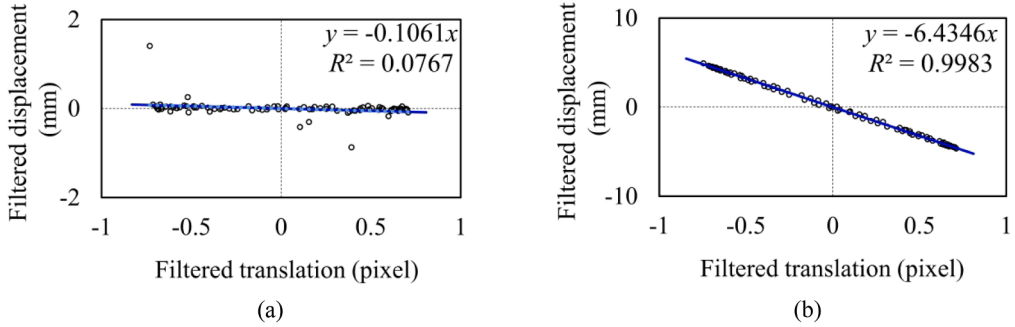


Fig. 19. Scale factors estimated using 100 Hz acceleration measurement and 3 Hz (aliased) vision measurements by (a) existing [16] and (b) proposed algorithms (Excitation 1: 0.1 Hz + 2.2 Hz).

accurately that was almost identical to that estimated using the 100 Hz acceleration and 30 Hz vision measurements. However, the existing algorithm did not estimate the scale factor accurately owing to temporal aliasing. Notably, the scale factor estimated by the proposed algorithm using 100 Hz acceleration and 3 Hz vision measurements (6.4346 pixels/mm) was used for further displacement estimation.

Subsequently, the HS displacements were estimated under different excitation conditions. The transition band of the complementary FIR filter was set to [0.5 Hz, 1.0 Hz], and therefore, the smallest sampling rate ($F_{min,l}$) required for vision measurement was 3 Hz. Fig. 20 shows a comparison of the displacements estimated by the proposed and existing techniques using 3 Hz vision and 100 Hz acceleration measurements, and Fig. 21 shows a comparison of their frequency spectra. The cut-off frequency was set to 1 Hz with an accuracy index of 0.97 for the existing technique [22]. In all five excitation cases, the proposed technique accurately estimated displacement with RMSEs less than 0.3 mm by explicitly eliminating temporally aliased errors in the vision-based displacement. The existing technique accurately estimated displacement under Excitation 5 because the aliased error in the vision-based displacement occurred at 1.3 Hz (>1 Hz), and then the error could be completely eliminated by the low-pass filter (Fig. 20(e) and Fig. 21(e)). For Excitations 1 and 3, aliased errors in vision-based displacements appeared at 0.8 Hz and 0.9 Hz, respectively, and fell into the transition band of the low-pass FIR filter, and then the errors were partially reduced, but not completely eliminated (Fig. 21(a) and (c)). Therefore, displacements were estimated using the existing technique with relatively larger RMSEs compared with that of the proposed technique (Fig. 20(a) and (c)). Because the frequencies of the aliased errors in vision-based displacements under Excitations 2 and 4 were smaller than 0.5 Hz, the aliased errors were completely retained in the final estimated HS displacements even after fusing with acceleration. Thus, large errors of approximately 2 mm were observed in the displacements estimated using the existing technique (Fig. 21(b) and (d)). In all five cases, the excitation frequencies identified by the proposed and existing techniques were identical to those identified from the reference displacements. However, the identified excitation frequencies were slightly different from the nominated excitation frequencies with a maximum error of 0.0074 Hz. Note that 54 s data with a sampling rate of 100 Hz were used here and then the frequency resolution is 0.0185 Hz for both the estimated and reference displacements.

Table 2 lists the RMSEs of displacements estimated by the proposed technique and the Kalman filter-based technique developed earlier by the authors [16]. The proposed technique outperformed the Kalman filter-based technique in all five cases at the cost of a time delay (2.5 s). Note that the Kalman filter-based technique did not include any smoothing algorithms, and thus estimated displacement in real-time.

5.1.3. Effect of the sampling rate of the vision measurement on displacement estimation performance

Additionally, the effect of the sampling rate of the vision measurement on displacement estimation performance was investigated

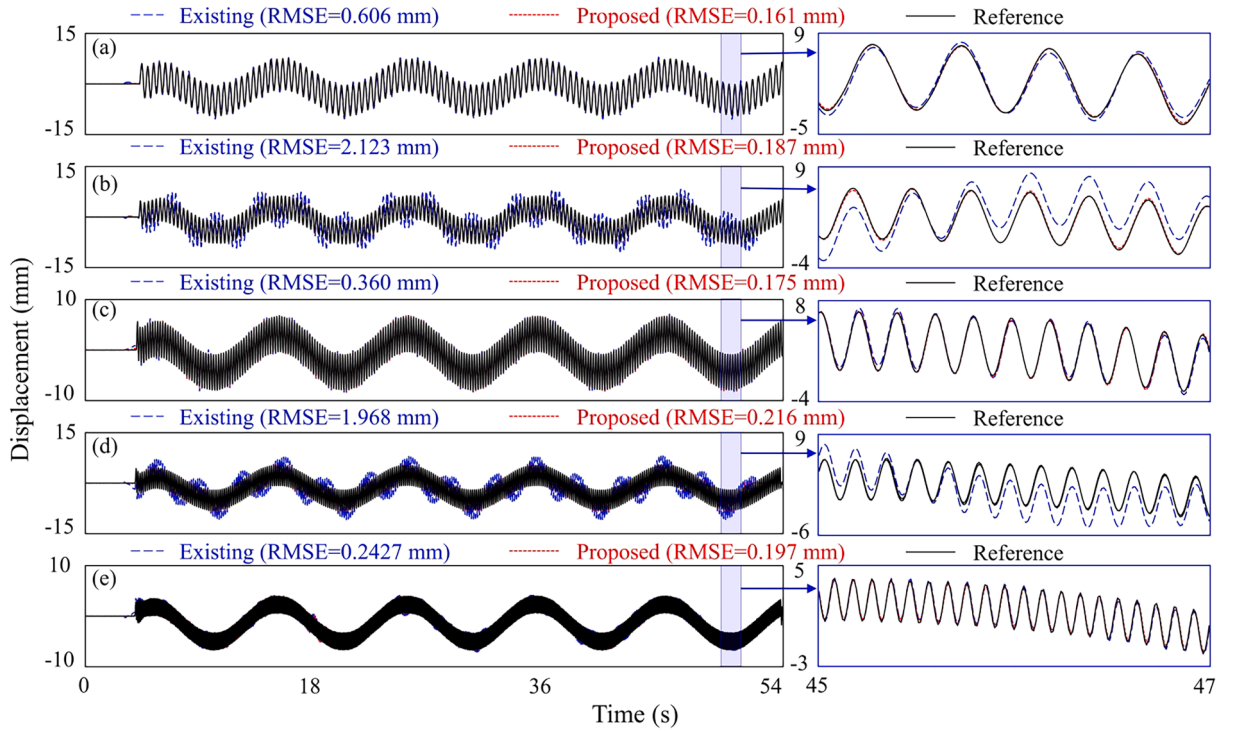


Fig. 20. Comparison of single-story building displacements estimated by the existing [22] and proposed techniques using 100 Hz acceleration and 3 Hz vision measurements: (a) Excitation 1: 0.1 Hz + 2.2 Hz, (b) Excitation 2: 0.1 Hz + 3.3 Hz, (c) Excitation 3: 0.1 Hz + 5.1 Hz, (d) Excitation 4: 0.1 Hz + 6.3 Hz, and (e) Excitation 5: 0.1 Hz + 10.3 Hz.

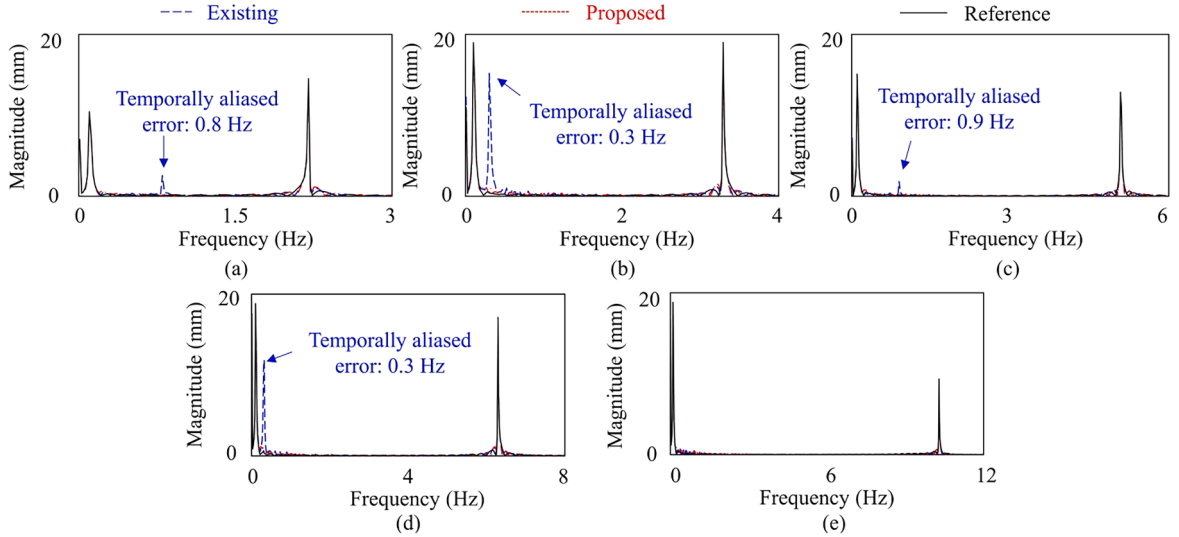


Fig. 21. Comparison of frequency spectra of single-story building displacements estimated by the existing [22] and the proposed techniques using 100 Hz acceleration and 3 Hz vision measurements: (a) Excitation 1: 0.1 Hz + 2.2 Hz, (b) Excitation 2: 0.1 Hz + 3.3 Hz, (c) Excitation 3: 0.1 Hz + 5.1 Hz, (d) Excitation 4: 0.1 Hz + 6.3 Hz, and (e) Excitation 5: 0.1 Hz + 10.3 Hz.

by fusing a 100 Hz acceleration measurement with the vision-based displacement with a sampling rate varying from 30 Hz to 3 Hz. Table 3 summarizes the frequencies of the aliased errors in vision-based displacement with different sampling rates, and they were categorized into three types: (1) no temporal aliasing, (2) temporally aliased error in the low-frequency band (< 1 Hz), and (3) temporally aliased error in the high-frequency band (≥ 1 Hz).

The RMSEs of the displacements estimated using the existing FIR based technique [22], the existing Kalman filter based technique

Table 2

RMSEs of displacement estimated by the Kalman filter-based technique previously developed by the authors [16] and the proposed technique (Unit: mm).

| # of excitations | Kalman filter-based technique [16] | Proposed technique |
|------------------|------------------------------------|--------------------|
| 1 | 0.819 | 0.161 |
| 2 | 0.851 | 0.187 |
| 3 | 0.821 | 0.175 |
| 4 | 0.946 | 0.216 |
| 5 | 0.782 | 0.197 |

Table 3

Frequency of the aliased errors in LS vision-based displacements of the single-story building model.

| Vision sampling rate $F_{s,v}$ (Hz) | Excitation signals | 0.1 Hz + 2.2 Hz | 0.1 Hz + 3.3 Hz | 0.1 Hz + 5.1 Hz | 0.1 Hz + 6.3 Hz | 0.1 Hz + 10.3 Hz |
|-------------------------------------|--|-----------------|----------------------|-----------------|-----------------|---|
| 30 | | 0.1 Hz + 2.2 Hz | No temporal aliasing | | | |
| 15 | | | | | | 4.7 Hz |
| 10 | | | | 4.9 Hz | 4.7 Hz | 0.3 Hz |
| 6 | | | 2.7 Hz | 0.9 Hz | 0.3 Hz | 1.7 Hz |
| 5 | | | 1.7 Hz | 0.1 Hz | 1.3 Hz | 0.3 Hz |
| 3 | 0.8 Hz low-frequency aliasing error | 0.3 Hz | 0.9 Hz | 0.3 Hz | 0.3 Hz | 1.3 Hz high-frequency aliasing error |

[16], and the proposed techniques are compared in Fig. 22. The existing FIR filter-based technique performs better than the Kalman filter-based technique if no temporal aliasing occurs, but worse if temporal aliasing occurs. However, the proposed technique always performs better than both techniques with less than 0.3 mm errors. In addition, the displacement estimation accuracy of the proposed technique was not very sensitive to the sampling rate of vision-based displacement and a TLS vision measurement could be used to reduce the computational costs and power assumption. This is important for developing a wireless visual-inertial sensor platform for continuous displacement monitoring.

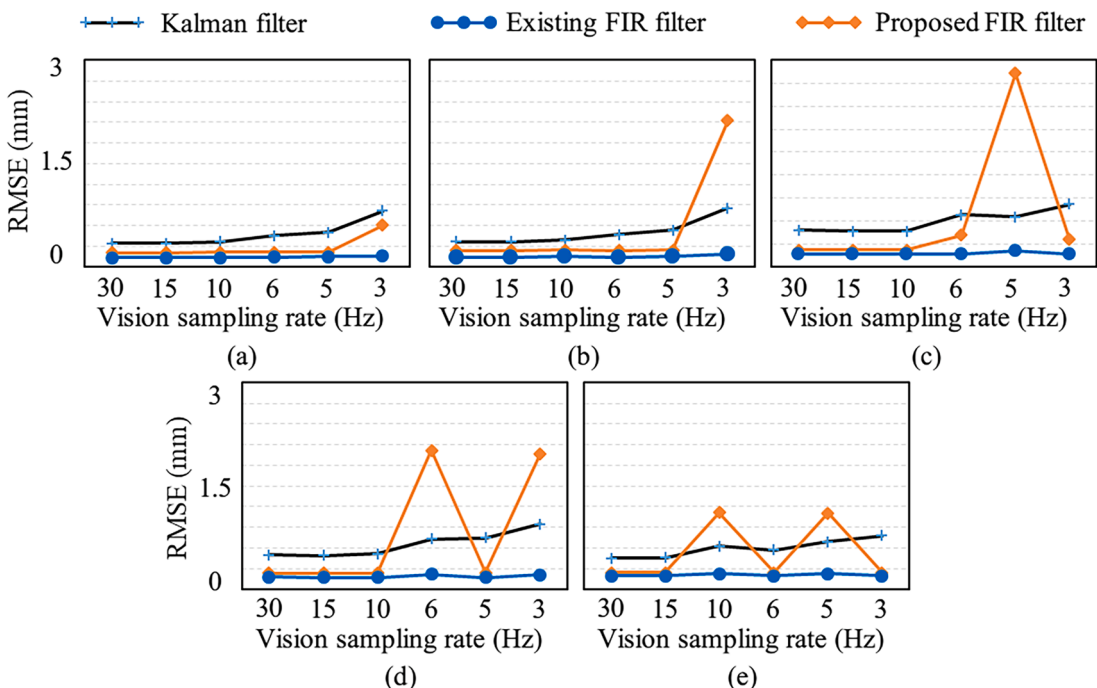


Fig. 22. Comparison of RMSEs of displacement estimated by the Kalman filter-based technique, existing FIR-based technique, and the proposed FIR-filter based technique with different vision sampling rate: (a) Excitation 1: 0.1 Hz + 2.2 Hz, (b) Excitation 2: 0.1 Hz + 3.3 Hz, (c) Excitation 3: 0.1 Hz + 5.1 Hz, (d) Excitation 4: 0.1 Hz + 6.3 Hz, and (e) Excitation 5: 0.1 Hz + 10.3 Hz.

5.1.4. Effect of spline interpolation employed in measurement alignment on displacement estimation performance

Finally, the effect of spline interpolation employed in measurement alignment on displacement estimation performance was investigated. The displacements were estimated using vision and acceleration measurements aligned with and without spline interpolation. Fig. 23 summarizes the RMSE reduction achieved by spline interpolation. The RMSE reduction was not evident when the vision measurement did/did not include any temporally aliased errors only in the high-frequency band (>1 Hz). This could be the reason for the existing studies to perform measurement alignment without interpolation [15]. However, the RMSEs were significantly reduced (up to 40 %) with temporally aliased errors in the low-frequency band (<1 Hz). This indicated that the anti-aliasing stage of the proposed technique was very sensitive to the measurement alignment error, and precise alignment between the vision and acceleration measurements was mandatory.

5.1.5. Additional test considering a large non-zero-mean excitation

Considering that actual structures usually have significant pseudo-static displacements, an additional test was conducted on the single-story building model. The experimental setup was the same as mentioned in Section 5.1.1. A 5.1 Hz sinusoidal signal was input into the shaker to generate high-frequency displacement for the model. At the same time, the model was manually pushed and released to generate large pseudo-static displacement. Fig. 24 shows displacements estimated by fusing 100 Hz acceleration measurement with the vision-based displacement with three different sampling rates (i.e., 3 Hz, 5 Hz, and 10 Hz). In all three cases, the proposed technique accurately estimated displacement with RMSEs of approximately 0.2 mm. The existing technique accurately estimated displacement when using 10 Hz vision-based displacement because the aliased error in the vision-based displacement at 4.9 Hz was completely eliminated by the low-pass filter. However, when using 3 Hz and 5 Hz vision-based displacements, the existing technique cannot or cannot fully eliminate aliased errors in the vision-based displacements. Therefore, the displacement estimation performance of the existing technique was worse than the proposed technique.

5.2. Pedestrian bridge test

5.2.1. Field test setup

A pedestrian bridge test was conducted to validate the proposed technique. As shown in Fig. 25, a uniaxial force balance accelerometer (EpiSensor ES-U2) and vision camera (Insta360 Pro 2) were installed at the 1/4 span point of the bridge. A Polytech RSV-150 LDV was installed on the ground to measure the true ground displacement with a resolution of less than 1μ m [40]. A joint of a traffic light support structure located at a distance of approximately 2 m was selected as a natural target, and an initial ROI was selected to include this target, as shown in Fig. 25(b). Three different excitations (that is, Excitations 1, 2, and 3) were considered in this test and the detailed description of these three excitations are listed in Table 4.

5.2.2. Scale factor and displacement estimation results

First, vision and accelerometer measurements were aligned using the proposed calibration algorithm, and the scale factor was estimated to be 1.345 pixel/mm from 3 Hz vision and 100 Hz acceleration measurements under Excitation 3. Next, the HS displacements were estimated using 3 Hz vision and 100 Hz acceleration measurements. Fig. 26 shows the displacement estimation results. The proposed technique achieved a more accurate displacement estimation than the existing technique [22] with an RMSE reduction of up to 64 %. Note that the improvement of the proposed methods lies in the elimination of temporally-aliased errors in the low-sampling vision-based displacement. However, the pedestrian bridge displacement under excitation 2 estimated from 3 Hz vision

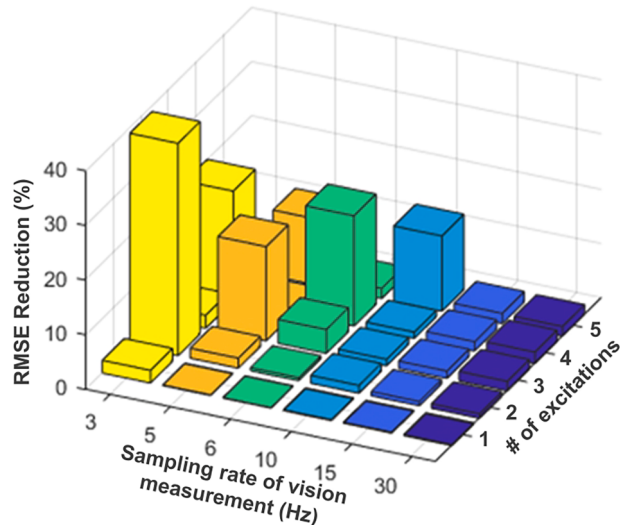


Fig. 23. RMSE reduction achieved using spline interpolation in measurement alignment.

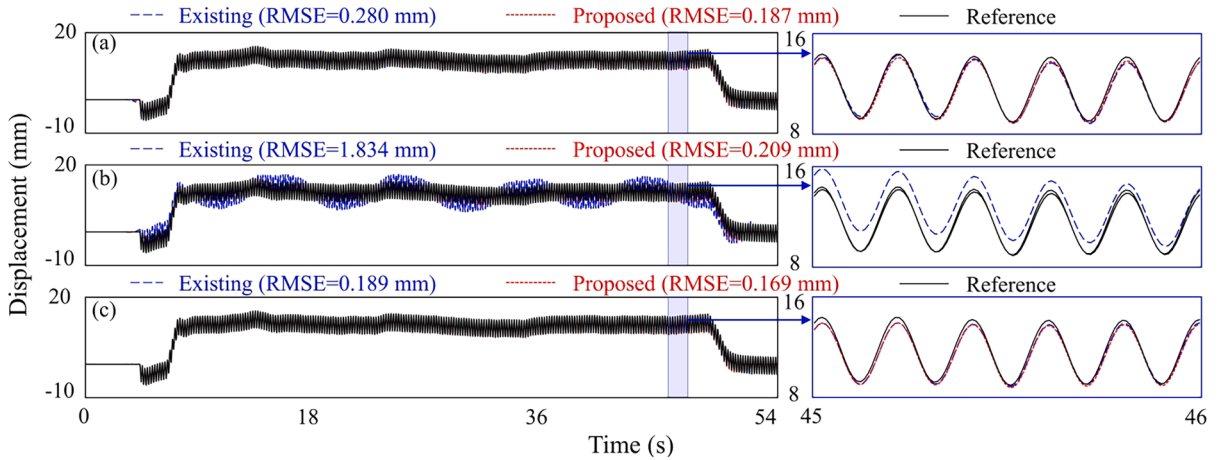


Fig. 24. Comparison of single-story building displacements estimated by the existing [22] and proposed techniques using: (a) 100 Hz acceleration + 3 Hz vision-based displacement, (b) 100 Hz acceleration + 5 Hz vision-based displacement, and (c) 100 Hz acceleration + 10 Hz vision-based displacement (Excitation: pseudo static + 5.1 Hz).

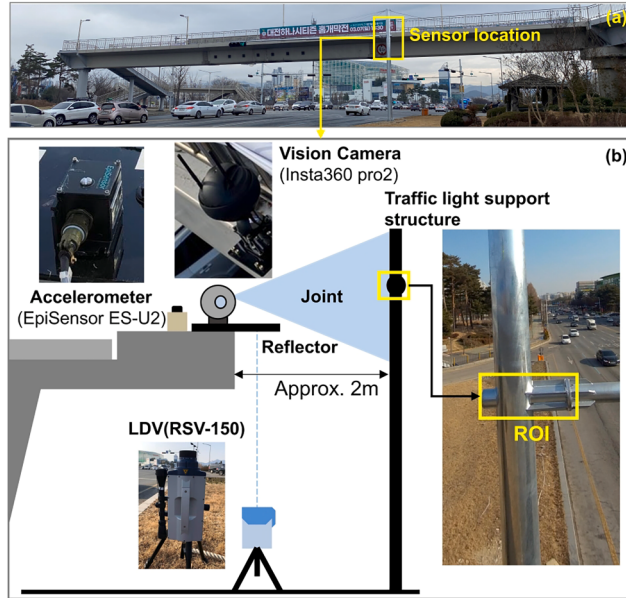


Fig. 25. Overall configuration of a pedestrian bridge test: (a) overview of the bridge and (b) sensor setup.

Table 4

Detailed description of three different excitations considered in the pedestrian bridge test.

| # of excitations | Descriptions |
|------------------|--|
| 1, 2 | 16 people slowly crossing the bridge and 2 people jumping at one-fourth span point |
| 3 | Four people jumping at one-fourth span point |

measurements had almost no aliasing errors. Therefore, the improvement of the proposed technique is neglectable as shown in Fig. 26 (b).

5.2.3. Effect of the sampling rate of vision measurement on displacement estimation performance

The performance of the proposed technique was further investigated by estimating the displacement by the fusion of 100 Hz acceleration and downsampled vision measurement. The vision measurement initially sampled at 30 Hz was downsampled by a factor

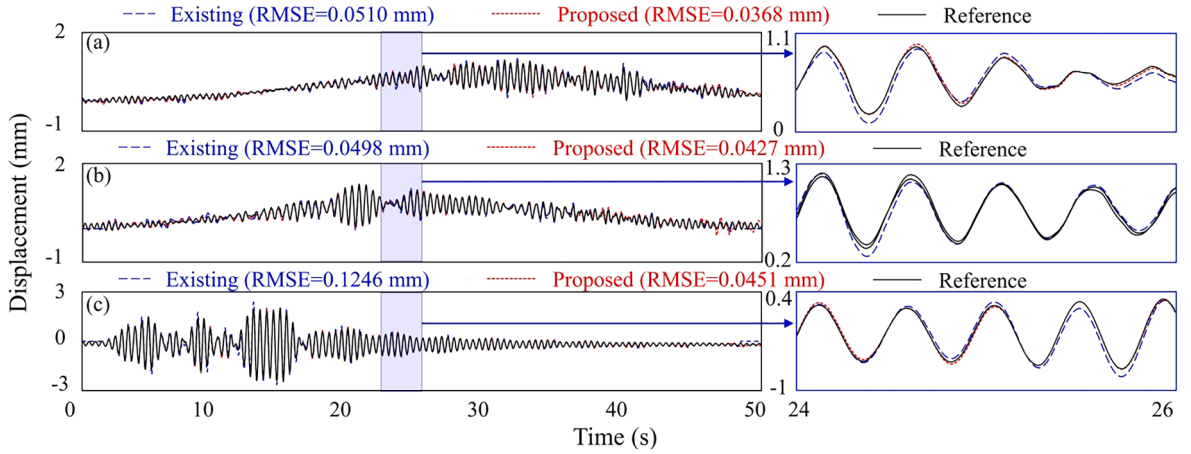


Fig. 26. Comparison of pedestrian bridge displacement estimated using the existing [22] and proposed techniques: (a) Excitation 1, (b) Excitation 2, and (c) Excitation 3.

(N) varying from 1 to 61. Then, the sampling rate of the downsampled vision measurement became $(30/N)$ Hz. Fig. 27 summarizes the RMSEs of the estimated displacements. Compared with the existing technique [22], the proposed technique showed less sensitivity to the sampling rate of vision measurement, and displacements were estimated with a similar error level. The existing technique had an estimation performance similar to that of the proposed technique with N below 9. Thereafter, increasing N (that is, downsampling) led to large RMSEs for the existing technique; this was attributed to the temporal aliasing issue.

Notably, the smallest sampling rate required for vision measurement is 3 Hz ($N = 10$) according to Eq. (1). With a sampling rate below 3 Hz, the transition bandwidth of P_H became considerably smaller, that is, less than 0.5 Hz. The high-pass filter of the complementary filters was then directly used as an anti-aliasing filter ($P_H = Q_H$). In such cases, the estimated displacement is suppressed in the frequency range of [0.5 Hz, 1 Hz], and temporally aliased errors induced by vision-based displacement in this frequency range cannot be correctly removed, resulting in inaccurate displacement estimation. However, most bridges have a pseudo-static displacement with a frequency below f_{pseudo} and a dynamic displacement with a frequency above their first natural frequency (f_1). There is no or a weak displacement response between these two frequencies. For the investigated pedestrian bridge, f_{pseudo} was less than 0.5 Hz, and f_1 was larger than 1 Hz, as shown in Fig. 28. Therefore, its displacement could still be accurately estimated using the proposed technique, even if the sampling rate of the vision measurement was less than 3 Hz. Fig. 27 shows that the proposed technique could accurately estimate the displacement using vision measurement with a sampling rate as low as 0.5 Hz ($N = 60$). One example is shown in Fig. 28 in which displacements were estimated under Excitation 3 using 1 Hz vision and 100 Hz acceleration measurements. A much large error was observed from the displacement estimated by the existing technique as shown in Fig. 28(a). The frequency spectrum of the displacement estimated using the proposed technique was in good agreement with that of the reference displacement, and identical frequency peaks (i.e., 2 Hz, 2.102 Hz, 2.224 Hz, and 2.51 Hz) were identified from the estimated and reference displacement. The same frequency peaks were identified from the frequency spectrum of the displacement estimated using the existing technique, but the temporally aliased errors at 0.082 Hz and 0.367 Hz were also clearly observed. Here, 49 s data with a sampling rate of 100 Hz were used and then the frequency resolution is 0.0204 Hz for both the estimated and reference displacements.

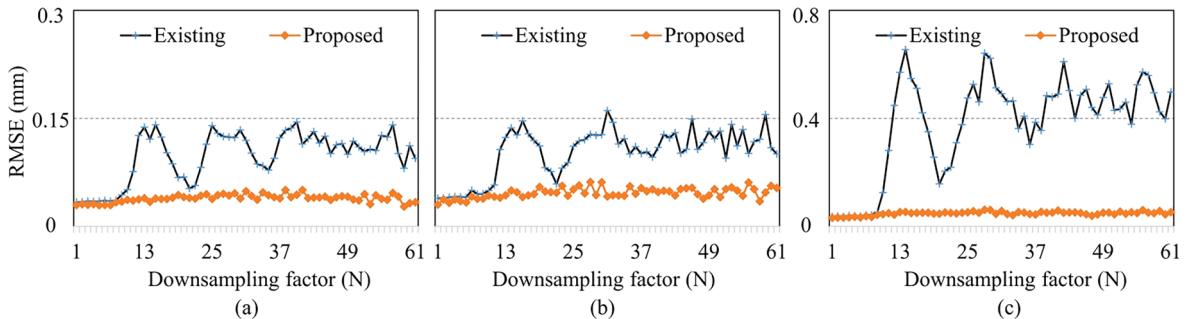


Fig. 27. Comparison of displacement estimation accuracy of the proposed and existing techniques using 100 Hz acceleration and downsampled vision measurements in the pedestrian bridge test: (a) Excitation 1, (b) Excitation 2, and (c) Excitation 3.

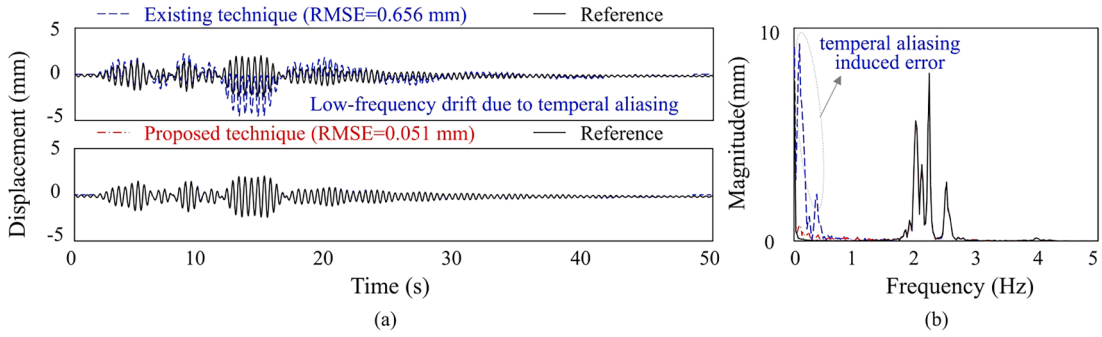


Fig. 28. Comparison of displacement estimated by the proposed and existing techniques under Excitation 3 using 1 Hz vision and 100 Hz acceleration measurements: (a) time domain and (b) frequency domain.

6. Conclusions

This study proposed an HS structural displacement estimation technique using the FIR filter-based fusion of HS acceleration and TLS displacement measurements. The temporally aliased error in the TLS displacement measurement was explicitly eliminated to ensure that the final estimated HS displacement was unaffected by the error. In addition, the proposed FIR filter-based two-stage fusion technique was applied to fuse a vision camera and an accelerometer. Automatic scale factor estimation and measurement alignment were achieved using the proposed initial calibration algorithm with short-period HS acceleration and TLS displacement measurements. The proposed technique was verified on a numerical simply supported beam model, a single-story building structure, and a pedestrian bridge, and the following conclusions were drawn:

- (1) In both numerical simulation and experimental validation, the proposed technique could eliminate the effect of the aliased error on displacement estimation accuracy, and an improvement in displacement estimation accuracy was achieved compared to the existing technique.
- (2) The scale factor for unit conversion was accurately estimated using the short-period HS acceleration and TLS vision measurements.
- (3) Precise alignment of vision and acceleration measurements was vital for the fusion of HS acceleration and TLS displacement measurements, and spline interpolation was necessary for measurement alignment.
- (4) With a sampling rate of displacement measurement above the minimum sampling rate defined by Eq. (1), the displacement estimation performance of the proposed technique was not very sensitive to the sampling rate of the displacement measurement.

Because the proposed technique does not require vision measurement sampled at a high rate, it is rather promising for implementation on a wireless sensor platform for continuous displacement monitoring. Efforts are underway to develop a displacement sensor module that integrates a photodetector for vision imaging, an accelerometer, and a microcontroller. In addition, the proposed technique was illustrated by estimating in-plane displacement only in one direction and could be easily extended to bi-directional in-plane displacement estimation. However, the existence of out-of-plane displacement or structural rotation may cause inaccurate in-plane displacement estimation, and future studies are warranted for three-dimensional structural displacement estimation and even six-degree-freedom structural displacement estimation.

Declaration of competing interest

The authors declare that they have no known competing financial interests or personal relationships that could have appeared to influence the work reported in this paper.

Data availability

Data will be made available on request.

Acknowledgement

This work was supported by the National Research Foundation of Korea (NRF) grant funded by the Korean Government (MSIT) (No. 2017R1A5A1014883).

References

- [1] D. Hester, J. Brownjohn, M. Bocian, Y. Xu, Low cost bridge load test: Calculating bridge displacement from acceleration for load assessment calculations, *Eng. Struct.* 143 (2017) 358–374, <https://doi.org/10.1016/j.engstruct.2017.04.021>.
- [2] F. Gomez, J. Park, B.F. Spencer Jr., Reference-free structural dynamic displacement estimation method, *Struct. Control Health Monit.* 25 (2018) e2209.
- [3] S. Nakamura, GPS measurement of wind-induced suspension bridge girder displacements, *J. Struct. Eng.* 126 (2000) 1413–1419, [https://doi.org/10.1061/\(ASCE\)0733-9445\(2000\)126:12\(1413\)](https://doi.org/10.1061/(ASCE)0733-9445(2000)126:12(1413)).
- [4] S.-J. Chang, N.-S. Kim, Estimation of displacement response from FBG strain sensors using empirical mode decomposition technique, *Exp. Mech.* 52 (2012) 573–589, <https://doi.org/10.1007/s11340-011-9522-z>.
- [5] K. Helmi, T. Taylor, A. Zarafshan, F. Ansari, Reference free method for real time monitoring of bridge deflections, *Eng. Struct.* 103 (2015) 116–124, <https://doi.org/10.1016/j.engstruct.2015.09.002>.
- [6] D.V.Q. Rodrigues, D. Zuo, C. Li, Wind-induced displacement analysis for a traffic light structure based on a low-cost doppler radar array, *IEEE Trans. Instrum. Meas.* 70 (2021) 1–9, <https://doi.org/10.1109/TIM.2021.3098380>.
- [7] C. Gentile, G. Bernardini, An interferometric radar for non-contact measurement of deflections on civil engineering structures: laboratory and full-scale tests, *Struct. Infrastruct. Eng.* 6 (2010) 521–534, <https://doi.org/10.1080/15732470903068557>.
- [8] Y. Fukuda, M.Q. Feng, M. Shinozuka, Cost-effective vision-based system for monitoring dynamic response of civil engineering structures, *Struct. Control Health Monit.* 17 (2010) 918–936, <https://doi.org/10.1002/stc.360>.
- [9] T. Khuc, F.N. Catbas, Computer vision-based displacement and vibration monitoring without using physical target on structures, *Struct. Infrastruct. Eng.* 13 (2017) 505–516, <https://doi.org/10.1080/15732479.2016.1164729>.
- [10] L. Luo, M.Q. Feng, Edge-enhanced matching for gradient-based computer vision displacement measurement, *Comput.-Aid. Civil Infrastruct. Eng.* 33 (2018) 1019–1040, <https://doi.org/10.1111/mice.12415>.
- [11] D. Lydon, M. Lydon, S. Taylor, J.M. Del Rincon, D. Hester, J. Brownjohn, Development and field testing of a vision-based displacement system using a low cost wireless action camera, *Mech. Syst. Sig. Process.* 121 (2019) 343–358, <https://doi.org/10.1016/j.ymssp.2018.11.015>.
- [12] W.S. Chan, Y.L. Xu, X.L. Ding, W.J. Dai, An integrated GPS-accelerometer data processing technique for structural deformation monitoring, *J. Geod.* 80 (2006) 705–719, <https://doi.org/10.1007/s00190-006-0092-2>.
- [13] K. Kim, J. Choi, J. Chung, G. Koo, I.-H. Bae, H. Sohn, Structural displacement estimation through multi-rate fusion of accelerometer and RTK-GPS displacement and velocity measurements, *Measurement* 130 (2018) 223–235, <https://doi.org/10.1016/j.measurement.2018.07.090>.
- [14] Z. Ma, J. Chung, P. Liu, H. Sohn, Bridge displacement estimation by fusing accelerometer and strain gauge measurements, *Struct. Control Health Monit.* 28 (2021) e2733.
- [15] J.-W. Park, D.-S. Moon, H. Yoon, F. Gomez, B.F. Spencer Jr., J.R. Kim, Visual-inertial displacement sensing using data fusion of vision-based displacement with acceleration, *Struct. Control Health Monit.* 25 (2018) e2122.
- [16] Z. Ma, J. Choi, H. Sohn, Real-time structural displacement estimation by fusing asynchronous acceleration and computer vision measurements, *Comput.-Aid. Civil Infrastruct. Eng.* 37 (2022) 688–703, <https://doi.org/10.1111/mice.12767>.
- [17] Z. Ma, J. Choi, P. Liu, H. Sohn, Structural displacement estimation by fusing vision camera and accelerometer using hybrid computer vision algorithm and adaptive multi-rate Kalman filter, *Autom. Constr.* 140 (2022), 104338, <https://doi.org/10.1016/j.autcon.2022.104338>.
- [18] T. Wu, L. Tang, S. Shao, X. Zhang, Y. Liu, Z. Zhou, X. Qi, Accurate structural displacement monitoring by data fusion of a consumer-grade camera and accelerometer, *Eng. Struct.* 262 (2022), 114303, <https://doi.org/10.1016/j.engstruct.2022.114303>.
- [19] Z. Ma, J. Choi, L. Yang, H. Sohn, Structural displacement estimation using accelerometer and FMCW millimeter wave radar, *Mech. Syst. Sig. Process.* 182 (2023), 109582, <https://doi.org/10.1016/j.ymssp.2022.109582>.
- [20] A.I. Ozdagli, J.A. Gomez, F. Moreu, Real-time reference-free displacement of railroad bridges during train-crossing events, *J. Bridg. Eng.* 22 (2017) 04017073, [https://doi.org/10.1061/\(ASCE\)BE.1943-5592.000113](https://doi.org/10.1061/(ASCE)BE.1943-5592.000113).
- [21] Y.S. Shmaliy, S. Zhao, C.K. Ahn, Unbiased finite impulse response filtering: an iterative alternative to kalman filtering ignoring noise and initial conditions, *IEEE Control Syst. Mag.* 37 (2017) 70–89, <https://doi.org/10.1109/MCS.2017.2718830>.
- [22] Y.H. Hong, S.G. Lee, H.S. Lee, Design of the FEM-FIR filter for displacement reconstruction using accelerations and displacements measured at different sampling rates, *Mech. Syst. Sig. Process.* 38 (2013) 460–481, <https://doi.org/10.1016/j.ymssp.2013.02.007>.
- [23] J.-W. Park, S.-H. Sim, H.-J. Jung, Displacement estimation using multimetric data fusion, *IEEE-ASME Trans. Mech.* 18 (2013) 1675–1682, <https://doi.org/10.1109/TMECH.2013.2275187>.
- [24] Y. Yang, S. Nagarajaiah, Output-only modal identification by compressed sensing: Non-uniform low-rate random sampling, *Mech. Syst. Signal Process.* 56–57 (2015) 15–34, <https://doi.org/10.1016/j.ymssp.2014.10.015>.
- [25] Y. Yang, C. Dorn, T. Mancini, Z. Talken, S. Nagarajaiah, G. Kenyon, C. Farrar, D. Mascareñas, Blind identification of full-field vibration modes of output-only structures from uniformly-sampled, possibly temporally-aliased (sub-Nyquist), video measurements, *J. Sound Vib.* 390 (2017) 232–256, <https://doi.org/10.1016/j.jsv.2016.11.034>.
- [26] Z. Ma, J. Choi, J. Jang, O. Kwon, H. Sohn, Simultaneous estimation of submerged floating tunnel displacement and mooring cable tension through FIR filter based strain and acceleration fusion, *Struct. Control Health Monit.* 2023 (2023) e7803876.
- [27] C.E. Shannon, Communication in the Presence of Noise, *Proceedings of the IRE.* 37 (1949) 10–21. 10.1109/JRPROC.1949.232969.
- [28] EETimes, How to use undersampling, EE Times. (2006). <https://www.eetimes.com/how-to-use-undersampling/> (accessed September 8, 2023).
- [29] A. Oppenheim, R. Schafer, *Discrete-time signal processing*, 3rd edition, Pearson, Upper Saddle River, 2009.
- [30] Y.H. Hong, H.-K. Kim, H.S. Lee, Reconstruction of dynamic displacement and velocity from measured accelerations using the variational statement of an inverse problem, *J. Sound Vib.* 329 (2010) 4980–5003, <https://doi.org/10.1016/j.jsv.2010.05.016>.
- [31] Equiripple single-rate FIR filter from specification object - MATLAB equiripple, (n.d.). <https://www.mathworks.com/help/dsp/ref/equiripple.html> (accessed February 16, 2022).
- [32] H. Bay, T.uytelaars, L. Van Gool, SURF: Speeded Up Robust Features, in: A. Leonardis, H. Bischof, A. Pinz (Eds.), *Computer Vision – ECCV 2006*, Springer, Berlin, Heidelberg, 2006, pp. 404–417, https://doi.org/10.1007/11744023_32.
- [33] E. Rublee, V. Rabaud, K. Konolige, G. Bradski, ORB: An efficient alternative to SIFT or SURF, in: *2011 International Conference on Computer Vision*, 2011: pp. 2564–2571. 10.1109/ICCV.2011.6126544.
- [34] K. Brieckle, U.D. Hanebeck, Template matching using fast normalized cross correlation, in: *Optical Pattern Recognition XII*, SPIE, 2001, pp. 95–102, <https://doi.org/10.1117/12.421129>.
- [35] Cross-correlation - MATLAB xcorr, (n.d.). <https://www.mathworks.com/help/matlab/ref/xcorr.html> (accessed February 17, 2022).
- [36] A.K. Chopra, *Dynamics of structures: theory and applications to earthquake engineering*, 4th edition., Pearson, 2011.
- [37] W.-Y. He, P. Liu, H.-C. Cheng, Z.-B. Li, J.-Q. Bu, Displacement reconstruction of beams subjected to moving load using data fusion of acceleration and strain response, *Eng. Struct.* 268 (2022), 114693, <https://doi.org/10.1016/j.engstruct.2022.114693>.
- [38] Q. Zhou, Q.-S. Li, X.-L. Han, J.-W. Wan, K. Xu, Horizontal displacement estimation of high-rise structures by fusing strain and acceleration measurements, *J. Build. Eng.* 57 (2022), 104964, <https://doi.org/10.1016/j.jobe.2022.104964>.
- [39] Polytec GmbH, RSV-400 Scanning Vibrometer Datasheet, (2019). http://hysen.cafe24.com/wp-content/uploads/2019/10/OM_DS_PSV-400_2011_05_E.pdf (accessed October 9, 2021).
- [40] Polytec GmbH, RSV-150 Scanning Vibrometer Datasheet, (2019). <https://www.atecorp.com/products/polytec/rsv-150> (accessed March 24, 2022).